Turnitin Low cycle fatigue behavior

by alfonsus oki

Submission date: 02-Feb-2024 05:25PM (UTC+0700)
Submission ID: 2206776484
File name: heterogeneous_grain_structured_CoCrFeMnNi_high-entropy_alloy.pdf (24.98M)
Word count: 8969
Character count: 47482

International Journal of Fatigue 182 (2024) 108185

Contents lists available at ScienceDirect

International Journal of Fatigue

journal homepage: www.elsevier.com/locate/ijfatigue

Low cycle fatigue behavior and deformation mechanism of core–shell heterogeneous grain structured CoCrFeMnNi high-entropy alloy

Zhe Zhang [a,b,c,*], Xinyu Zhai [a], Lydia Anggraini [d], Bo Zhang [b], Yushan Ma [b], Kei Ameyama [e], Xu Chen [a,c]

[a] School of Chemical Engineering and Technology, Tianjin University, Tianjin 300350, China
[b] School of Mechanical Engineering, Ningxia University, Yinchuan 750021, China
[c] Zhejiang Institute of Tianjin University, Ningbo, Zhejiang 315201, China
[d] Study Program of Mechanical Engineering, Faculty of Engineering, President University, Bekasi, West Java 17550, Indonesia
[e] Department of Mechanical Engineering, Faculty of Science and Engineering, Ritsumeikan University, Shiga 525-8577, Japan

ARTICLE INFO

Keywords:
High-entropy alloy
Heterogeneous structure
Low cycle fatigue
Cyclic response
Deformation mechanism

ABSTRACT

Heterogeneous grain structured high-entropy alloys (HEAs) exhibit excellent strength-ductility synergy due to the peculiar grain structure topology. However, the understanding of cyclic response and deformation mechanism under low cycle fatigue (LCF) loading is still inadequate. Therefore, the LCF behavior and deformation mechanism of CoCrFeMnNi HEAs with a three-dimensional core-shell grain structure were investigated in this paper. The effects of core–shell network structure on cyclic response and fatigue life are revealed. The dislocations activity dominantly appears in the soft core regions prior to the hard shell region. The LCF resistance remains when the strain amplitude is below 0.5%.

1. Introduction

High-entropy alloys (HEAs) have a relatively high mixing entropy and lattice distortion energy due to a multi-principal element alloys system. Compared to conventional pure metals and alloys, HEAs exhibit unexpected properties, such as unprecedented mechanical properties and high fracture toughness at cryogenic temperatures, excellent corrosion resistance and good wear resistance, etc [1–4]. Nowadays, overcoming the trade-off between strength and ductility in HEAs has attracted world-wide attention. Compared with homogeneous ultrafine-grained (UFG) structure or nanograined (NG) structure, peculiar heterogeneous structure can provide an additional hetero-deformation induced (HDI) strain hardening, generating unprecedented mechanical properties [5–11]. Therefore, development of heterogeneous structure in HEAs has been an emerging trend for achieving superior strength-ductility synergy [12–18]. Multiple strengthening mechanisms, consisting of interface/grain boundary strengthening, precipitation strengthening, HDI strengthening, etc., generates the high strength and high ductility.

Owing to the good combination of strength and ductility, the heterogeneous structured HEAs are great potential candidates for engineering applications. However, alternative loading and temperature often induce fatigue failure in structural components [19,20]. Therefore, it is of great important to reveal the fatigue behavior and deformation mechanism of the heterogeneous structured HEAs. In the past few years, much attention has been paid on the investigation of fatigue behavior of homogeneous coarse-grained (CG) and UFG HEAs under high cycle fatigue (HCF) loading. Both dislocation slip and deformation twinning occurred in the CG CoCrFeMnNi HEAs under stress-controlled HCF tests. Fatigue cracks propagated along the deformation twins [21,22]. Tian et al. [23] investigated the high cycle fatigue resistance of UFG CoCrFeMnNi HEAs. Compared with CG samples ($d = 30$ μm), the fatigue limit of UFG samples ($d = 0.65$ μm) increased by approximately 40 %. It is noted that the increased tensile strength enhances the resistance to crack initiation, increasing the HCF fatigue limit [24,25].

However, the ductility of HEAs often deteriorates gradually with increasing strength, which may induce inferior low cycle fatigue (LCF) resistance [26,27]. Therefore, the investigations on the LCF behavior and deformation mechanism of HEAs have attracted attention in the past few years. The LCF behavior and deformation mechanism of CG CoCrFeMnNi HEAs have been reported [28,29]. Phase transformation is not significant during the whole LCF process. It is observed that the initial

* Corresponding author at: School of Chemical Engineering and Technology, Tianjin University, Tianjin 300350, China.
E-mail address: zhe.zhang@tju.edu.cn (Z. Zhang).

https://doi.org/10.1016/j.ijfatigue.2024.108185
Received 5 October 2023; Received in revised form 27 December 2023; Accepted 25 January 2024

cyclic hardening followed by cyclic softening before fatigue failure. The CoCrFeMnNi HEAs exhibit much better LCF life than 304 stainless steels at $\Delta\varepsilon/2 > 0.5$ %. Moreover, the cyclic induced microstructure evolution is dependent on the stain amplitude. Namely, planar slip bands dominantly form in CG CoCrFeMnNi HEAs at low strain amplitudes ($\Delta\varepsilon/2 <$ 0.3 %), while the increased strain amplitude promotes the formation of dislocation veins, walls, or cells. Picak et al. [30] compared the cyclic response and deformation mechanism of hot-extruded and equal channel angular pressing (ECAP) produced CoCrFeMnNi HEAs. It is noted that the UFG samples have much better LCF life than CG samples as the strain amplitude is below 0.4 %, which is related to the enhanced strength and fatigue resistance of UFG samples. Nevertheless, the continuously increased strain amplitude promotes rapidly cyclic softening effect, which induces the inferior LCF life of UFG samples. By contrast, Luo et al. [31] investigated the cyclic deformation mechanism and LCF life of fine-grained (FG) CoCrFeMnNi HEAs. As grain size decreases from 184 μm to 18 μm, activity of dislocations changes from planar slip to wavy slip-driven subgrain structures within the grains. Moreover, nano twins can form in FG samples during LCF process. Therefore, both grain refinement and twinning-induced cyclic deformation are thought to be beneficial to LCF resistance. Moreover, the carbides are harmful for LCF resistance of CoCrFeMnNi HEAs [32]. Until now, the current studies mainly focus on cyclic response and deformation mechanism of the HEAs with homogeneous grain structure and are expected to enhance the mechanical properties and LCF resistance by optimizing the grain size.

In recent years, it is valuable to note that the investigations of LCF behavior and deformation mechanism shift from homogeneous grain structured materials to heterogeneous grain structured materials. The LCF resistance and deformation mechanism of GNS materials, such as Cu [33,34] and stainless steels [35,36], have been reported. It is noteworthy that GNS Cu exhibits much better LCF resistance than both CG Cu and UFG/NG Cu. The GNS structure generates an inhomogeneous distribution of cyclic plastic strain under cyclic loading. Namely, cyclic plastic strain accumulates in some local region of the GNS layer, resulting in grain coarsening inside GNS layer. However, the strain amplitude has a significant role on LCF life in GNS stainless steels. Namely, the superior LCF resistance appears in GNS stainless steels as the strain amplitude is below 0.5 %. While, the LCF life of GNS stainless steels is lower than that of CG stainless steels at $\Delta\varepsilon/2 > 0.5$ %. In addition, LCF deformation mechanism of TRIP dual-phase HEAs are also reported. Compared with the CoCrFeMnNi HEA with simple FCC structure, dual-phase $Al_{0.5}$CoCrFeMnNi HEAs have inferior LCF at high strain amplitude ($\Delta\varepsilon/2 > 0.7$ %), which is related to the rapid crack initiation at BCC/FCC phase boundaries. Moreover, the activity of dislocations changes from planar slip to wavy slip with increasing strain amplitude [37]. Similarly, $Fe_{50}Mn_{30}Co_{10}Cr_{10}$ HEAs with metastable dual-phase (FCC + HCP) also show different LCF deformation mechanism with increasing strain amplitude [38]. Namely, deformation-induced martensitic transformation dominantly occurs in the FCC phase at $\Delta\varepsilon/2 < 0.6$ %, while deformation induced twinning dominantly occurs in the HCP and FCC phase at $\Delta\varepsilon/2 > 0.6$ %. Overall, heterogeneous structure design become an effective strategy to realize superior mechanical properties, i.e. great synergy of strength and ductility and good fatigue resistance. Although preliminary investigations of LCF behavior in the heterogenous structured materials have been investigated, the effects of grain structure topology and strain amplitude on LCF life and deformation mechanism are not clear. Especially, the understanding of LCF behavior and deformation mechanism of the heterogeneous grain structured HEAs is still inadequate.

A periodically macro-scale core–shell network structure is one of typical heterogenous structures, which is also termed as harmonic structure (HS) [39–41]. Compared with other heterogenous structures, the spherical CG structures (core) embed in a three-dimensional UFG network structure (shell) in the HS. Moreover, owing to the enhancement of strain hardening capability, the HS materials exhibit a good balance of high strength and high ductility [42–46]. The increased strength also enhances the HCF fatigue resistance. Deflection of fatigue crack grow path can be observed at the core/shell interfaces [47,48]. In recent years, the preparation and mechanical properties of the harmonic structured HEAs have been investigated. The HS CoCrFeMn and CoCrFeMnNi HEAs show a superior strength-ductility synergy [49,50]. However, it is noted that the stress concentration occurs at the core/shell interface and the resistance to fatigue crack propagation deteriorates in the UFG network structure, which plays an important role on fatigue resistance [51]. Preliminary investigations of LCF behavior of the HS CoCrFeMnNi HEAs were carried out at a strain amplitude of 0.5 % [50]. It is noteworthy that although the ductility reduces with increasing shell fraction, the HS samples still show the similar fatigue life with CG samples, indicating that the peculiar core–shell network structure has unexpected effect on the LCF resistance. As mentioned above, the strain amplitude also has a significant influence on LCF life and deformation mechanism of HEAs. However, the combined effects of strain amplitude and core–shell network structure topology on LCF behavior and deformation mechanism in HEAs are still unclear.

The CoCrFeMnNi HEA exhibits a stable face-centered-cubic (FCC) structure during monotonic and cyclic deformation at room temperature [50,51]. Therefore, the LCF behavior and deformation mechanism of the HS CoCrFeMnNi HEAs having different shell fractions are investigated in the present work. The combined effects of strain amplitude and shell fraction on cyclic response and LCF life are clarified. Moreover, the cyclic deformation mechanism and fatigue fracture of the peculiar core–shell network structure are revealed. Our investigations may provide further insights into the LCF behavior of the heterogeneous structured HEAs.

2. Experiments

Commercial gas-atomized CoCrFeMnNi HEA powder (Cr:19.00 %, Mn: 20.47 %, Fe: 19.53 %, Co: 20.60 %, Ni: 20.40 %, N: 0.0074 %, O: 0.0359 %) ranging from 45 ~ 105 μm was used to fabricate the HS CoCrFeMnNi HEAs. Firstly, the initial powders were mechanical milled (MM) by a planetary ball mill under argon atmosphere at room temperature. The mass ratio of ball-powder was 10:1, and milling speed was 200 r/min. Then, the powders were sintered by spark plasma sintering (SPS) process under 50 MPa at 950 °C for 10 min. The diameter of the sintered compacts was approximately 15 mm. MM0h, MM40h, MM100h are termed as the sintered compacts produced from initial powders and powders milled for 40 h and 100 h, respectively.

Tensile test was carried out by an in-situ fatigue testing system (CARE IBTC-5000) at room temperature. The strain was measured by a digital image correlation (DIC) based video extensometer (Imetrum, UK). A constant tensile strain rate of 3.3×10^{-3}/s (a constant cross-head speed of 0.01 mm/s) was performed. Gauge length and cross-section of the tensile specimen were 3 mm and 1 mm × 1 mm, respectively. Moreover, symmetrical strain-controlled LCF tests were performed under the same fatigue testing system with a constant triangular wave loading rate of 5×10^{-3}/s. According to the previous literature [50], the LCF specimen had a gauge length of 2.1 mm and a cross-section of 1 mm × 1 mm. The strain amplitudes of 0.3 %, 0.4 %, 0.5 %, and 0.7 % were performed, respectively. The number of cycles at 50 % peak stress in the stable softening region was determined as the LCF life. At least three specimens were measured for verify the repeatability of the results. The surface of specimens was ground using 2000 grit SiC paper before tests.

The grain structure of the sintered compacts was observed by an optical microscope (OM, Keyence VHX-900) and a scanning electron microscope (SEM, FEI Apreo S Lo Vac) equipped with an electron backscattering diffraction detector (EBSD, EDAX) operating at 20 kV. The fatigue crack initiation in the deformed specimens was also characterized by SEM. Moreover, the morphology of dislocations was examined by a transmission electron microscope (TEM, FEI Talos-F200X) operating at 200 kV.

3. Results

3.1. Microstructure and mechanical properties

Fig. 1 shows the grain structure of the sintered CoCrFeMnNi HEAs. It is seen from Fig. 1a and 1d that the MM0h sample has a CG structure with an average grain size of approximately 11.84 μm. By contrast, UFG structure forms in the MM40h samples, and its fraction is approximately 20.3 % (see Fig. 1b and 1e). The CG grain size of MM40h samples is approximately 8.14 μm, while the UFG grain size is approximately 1.01 μm. As milling time increases to 100 h, the fraction of UFG structure increases significantly, which is approximately 46.8 % (see Fig. 1c and 1f). However, the reduction of grain size is not significant as the milling time increases. The CG grain size and UFG grain size of MM100h samples are approximately 6.98 μm and 0.77 μm, respectively. Overall, the grain size in CG structure or UFG structure decreases slightly, but the UFG fraction increases significantly with increasing milling time. Usually, slight oxidation exists in the powder surface during fabrication process. The HS CoCrFeMnNi HEAs were produced by mechanical milling and powder metallurgy. Based on the previous works [50,51], although a few nano oxide particles can be observed in the sintered compacts, they had little influence on crack initiation and propagation. The effect of oxide particles on LCF failure is ignored in the present work.

It is noteworthy that the UFG structure in the MM40h and MM100h CoCrFeMnNi HEAs exhibits a clear network structure, indicating that the harmonic structure is produced. The CG structure is denoted as core region, while the UFG structure is shell region. Moreover, the enlarged microstructure of shell region is shown in Fig. 2. It is noted that the grain size distribution in the shell region is inhomogeneous. As indicated in Fig. 2b and Fig. 2d, the gain size in the center of the shell region is below 1 μm, while the grain size is approximately 1 ~ 3 μm in the narrow region near the core/shell interface. The schematic of shell region of the harmonic structured CoCrFeMnNi HEAs is shown in Fig. 2e. It has been reported that the phase transformation can promote the grain refinement, thus the HS SS304L steels show a sharp core/shell interface [42,43]. On the contrary, the phase transformation is not significant during the milling and sintering of CoCrFeMnNi HEAs powders. Therefore, the HS CoCrFeMnNi HEAs have the continuous network and gradient UFG structure. Similarly, the gradient shell region is also observed in HS Ni without significant phase transformation [52].

The microstructure and tensile results of the sintered CoCrFeMnNi HEAs are shown in Fig. 3. Fig. 3a shows the variation of grain size and shell fraction in the sintered samples with increasing mechanical milling time. The tensile stress–strain curves of the sintered samples with different microstructures are shown in Fig. 3b. It is seen that both yield strength and ultimate tensile strength of the HS sample with $S_f = 20.3$ % increase by approximately 100 MPa compared with CG samples ($S_f = 0$ %). Meanwhile, the elongation of the HS sample with $S_f = 20.3$ % reduces only by 4 %. Thus, the HS sample with $S_f = 20.3$ % shows a good synergy of strength and ductility. However, when the shell fraction continuously increases from 20.3 % to 46.8 %, the strength of the HS sample increases by approximately 100 MPa, but the elongation reduces by approximately 18 %, indicating the ductility deteriorates significantly.

3.2. Cyclic response and fatigue life

Fig. 4 shows the cyclic stress response of the HS CoCrFeMnNi HEAs under different strain amplitudes. It is seen from Fig. 4a to 4c that both CG samples and HS samples show similar cyclic stress response. Namely, the initial cyclic hardening occurs in the initial 10 cycles, and cyclic softening occurs with continuously increasing cycles. As expected, the larger strain amplitude generates the higher cyclic stress. Moreover, the

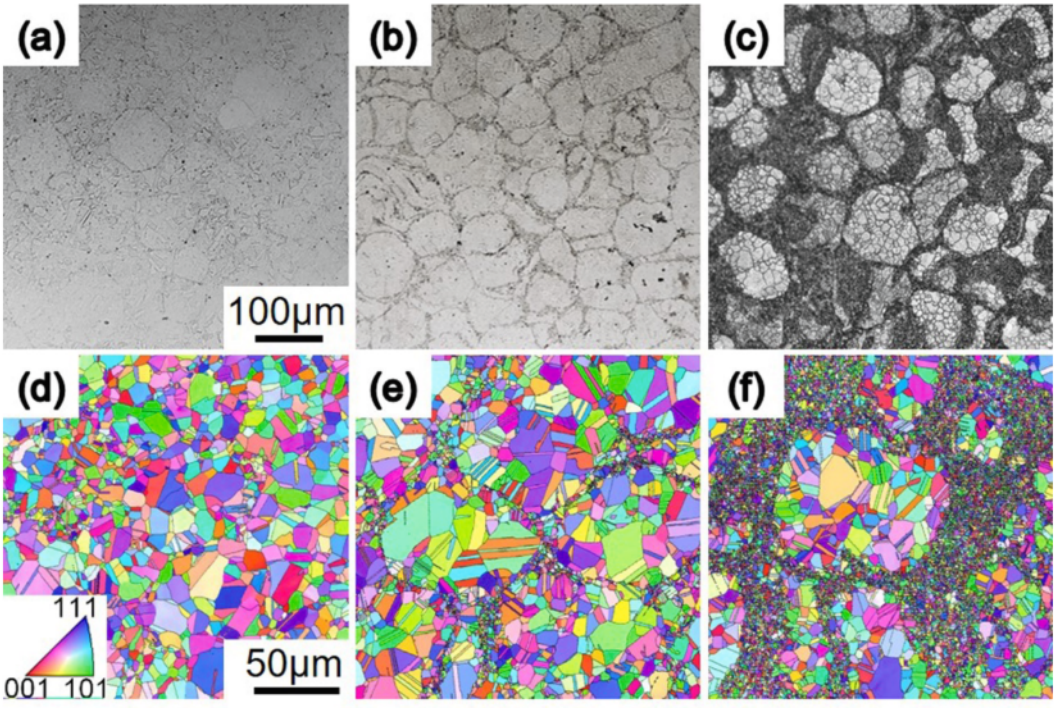

Fig. 1. The microstructure of the sintered CoCrFeMnNi HEAs: (a, d) MM0h samples, $S_f = 0$ %; (b, e) MM40h samples, $S_f = 20.3$ %; (c, f) MM100h samples, $S_f = 46.8$ %. (a-c) OM images, (d-f) EBSD images. S_f- Fraction of UFG region.

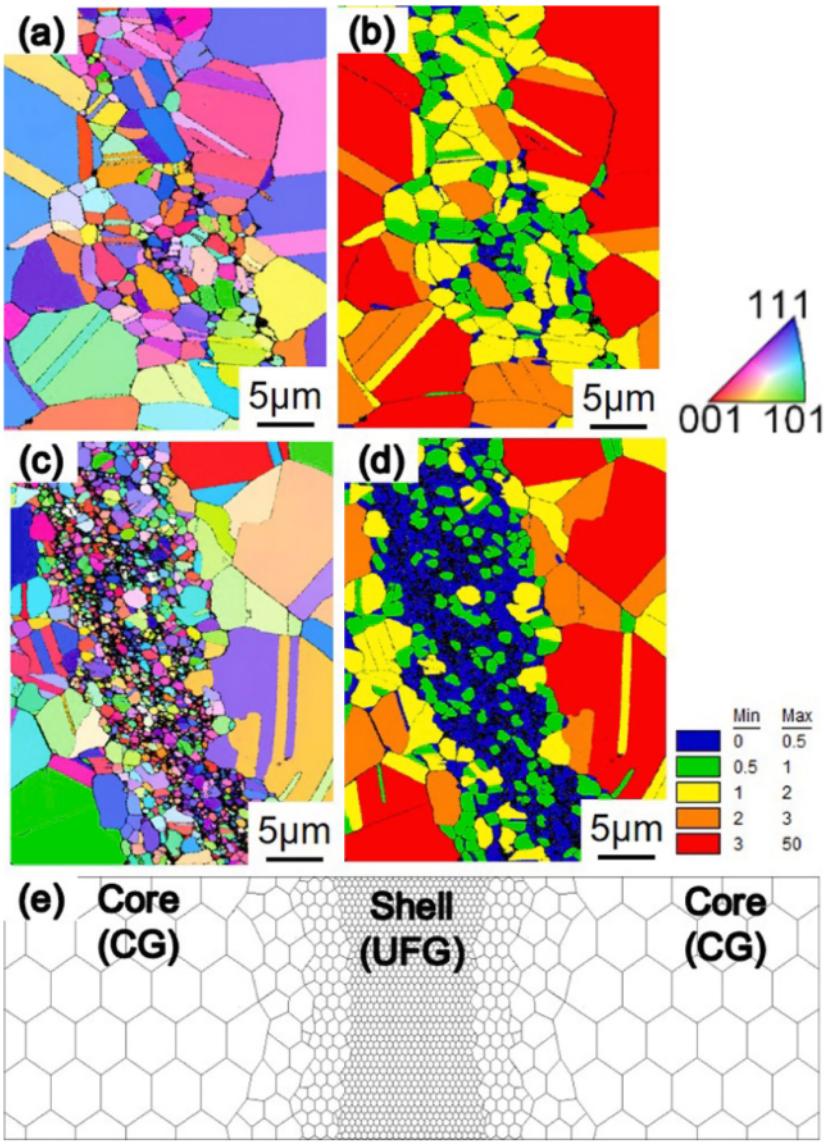

Fig. 2. Enlarged shell region of HS CoCrFeMnNi HEAs using EBSD: (a, b) MM 40 h samples; (c, d) MM 100 h samples; (e) Schematic of the gradient shell region.

cyclic stress amplitude also increases with increasing shell fraction under the same strain amplitude, which is attributed to the enhanced tensile strength of the HS samples.

To quantitively compare the differences of cyclic stress response of HEA samples with different shell fractions, the cyclic hardening rate (CHR) and cyclic softening rate (CSR) are defined in the Eq. (1) and Eq. (2), respectively [53].

$$CHR = \frac{\sigma_{\max} - \sigma_1}{\sigma_1} \tag{1}$$

$$CSR = \frac{\sigma_{\max} - \sigma_H}{\sigma_H} \tag{2}$$

where σ_1 is the peak cyclic stress in the first cycle, σ_{max} is the maximum peak cyclic stress in the following cycles, and σ_H is the peak cyclic stress in the half-life cycle. Fig. 5a and Fig. 5b show the CHR and CSR of the HS CoCrFeMnNi HEAs under different strain amplitudes, respectively. Overall, both CG samples and HS samples show an increased CHR and a decreased CSR with increasing strain amplitude. It is noted that the CHR decreases significantly with increasing shell fraction. On the contrary, the difference of CSR between CG samples and HS samples is not significant. It indicates that the shell fraction plays much more important role on initial cyclic hardening than cyclic softening.

Fig. 6 shows the half-life hysteresis loops of the HS CoCrFeMnNi HEAs under different strain amplitudes. It is seen that the shell fraction has significant influence on half-life hysteresis loops as the strain amplitude increases from 0.3 % to 0.7 %. As illustrated in Figs. 3 and 4, the yield strength of the HS samples increases significantly with increasing shell fraction, which also generates the increase of peak cyclic stress. Simultaneously, the increased yield strength enhances elastic behavior in the hysteresis loop, reducing the plastic strain amplitude. Thus, it is seen from Fig. 6 that the half-life hysteresis loop becomes slim

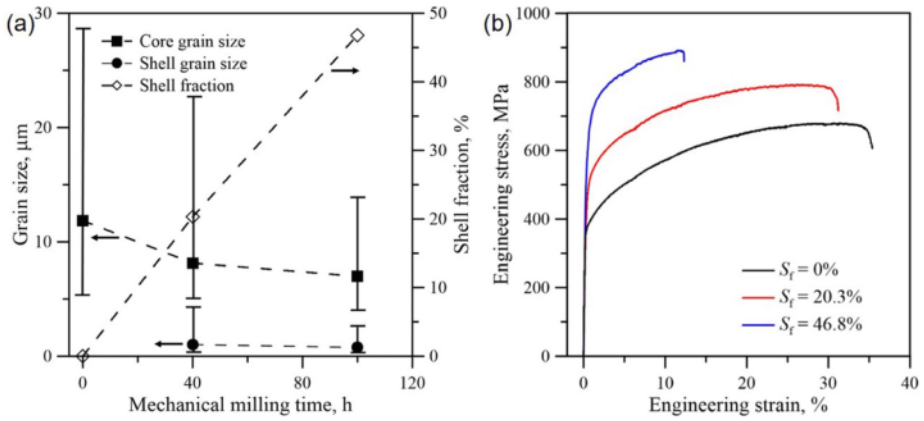

Fig. 3. (a) Microstructure evolution and (b) tensile results of the sintered CoCrFeMnNi HEAs.

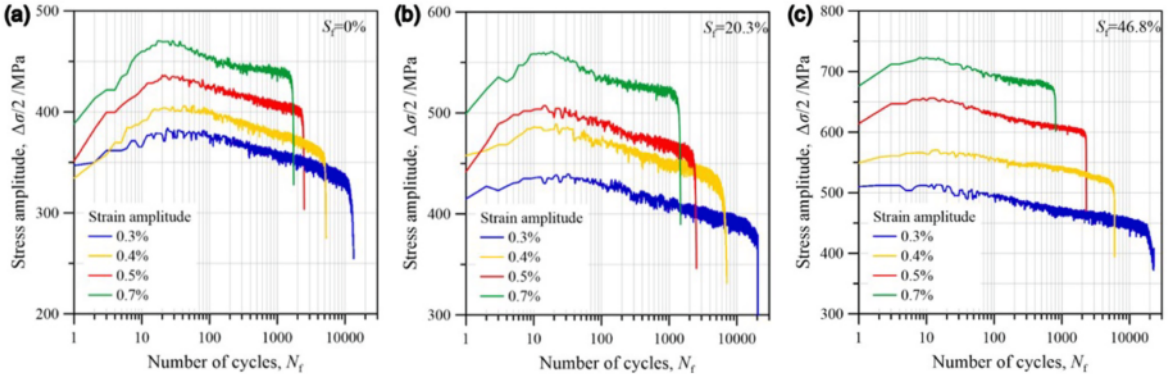

Fig. 4. Cyclic stress response of the HS CoCrFeMnNi HEAs with different microstructures: (a) S_f = 0 %; (b) S_f = 20.3 %; (c) S_f = 46.8 %.

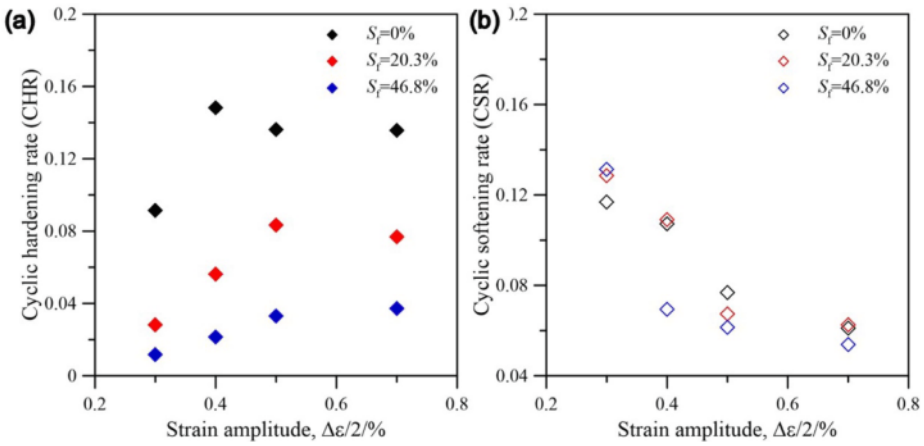

Fig. 5. Cyclic hardening and softening behavior of the HS CoCrFeMnNi HEAs with different microstructures: (a) Cyclic hardening rate; (b) Cyclic softening rate.

with increasing shell fraction under the same strain amplitude. The similar tendency is also reported in the grain-refined CoCrFeMnNi HEA with homogeneous grain structure [30].

The analysis of the stress–strain hysteresis loop is very valuable to provide primary or fundamental information about the interaction between the applied load and the microstructural processes of the material [54]. Masing behavior is well-known to study deformation behavior upon stress reversal, which is defined by comparing the shapes of hysteresis loops with the cyclic stress–strain curve. If the shape of the loop matches with the cyclic stress–strain curve (stress ordinate

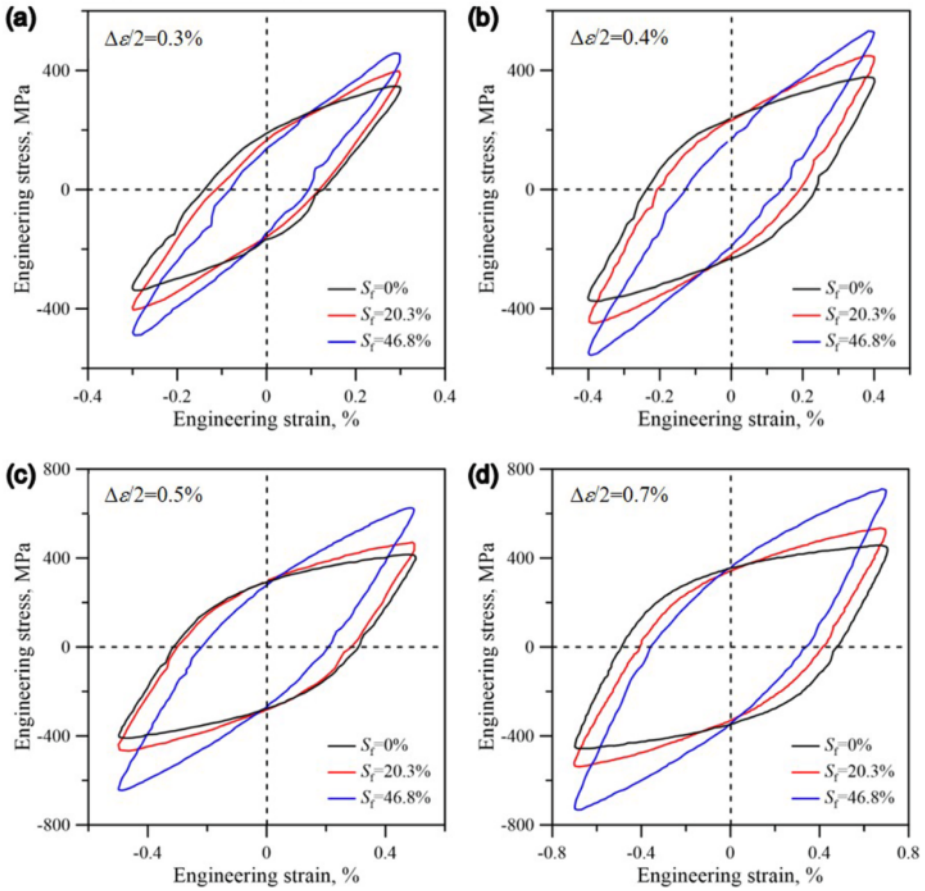

Fig. 6. Half-life hysteresis loops of the HS CoCrFeMnNi HEAs under different strain amplitudes: (a) $\Delta\varepsilon/2 = 0.3$ %; (b) $\Delta\varepsilon/2 = 0.4$ %; (c) $\Delta\varepsilon/2 = 0.5$ %;(d) $\Delta\varepsilon/2 = 0.7$ %.

multiplied by two), then the Masing behavior appears. Otherwise, if these two curves do not match, then the non-Masing behavior appears [55]. The effect of shell fraction on Masing behavior of HS CoCrFeMnNi HEAs is illustrated in Fig. 7. It is seen from Fig. 7a that the CG sample exhibits obvious non-Masing behavior. By contrast, the non-Masing behavior become weak as the shell fraction increases to 20.3 % (see Fig. 7b). It is noted from Fig. 7c that near Masing-behavior is observed in the HS sample with $S_f = 46.8$ %. It is reported that the Masing-behavior is dependent on dislocation arrangements [30,56]. In the present work, compared with CG sample, the near Masing-behavior displays in the HS samples with high shell fraction, indicating the alternation of the dislocation arrangements. The further investigations on microstructure evolution are discussed in the following section.

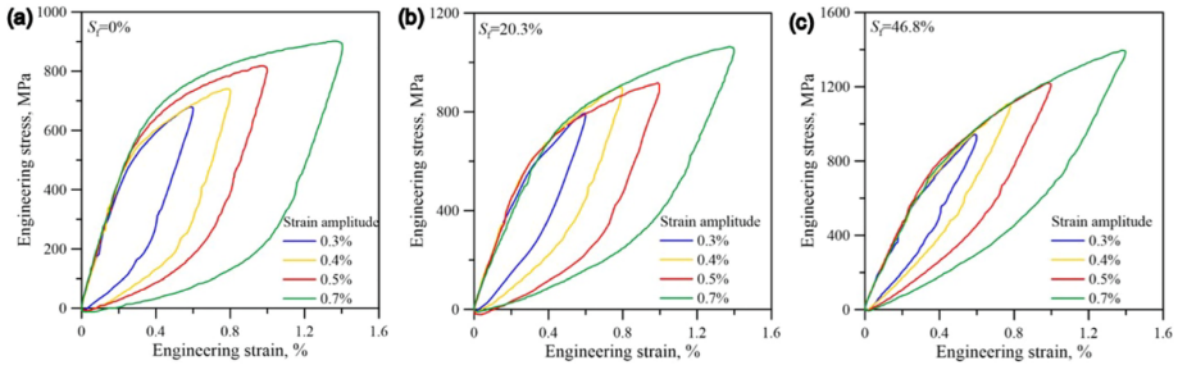

Fig. 7. Half-life hysteresis loops plotted in relative coordinates: (a) $S_f = 0$ %; (b) $S_f = 20.3$ %; (c) $S_f = 46.8$ %.

3.3. Low cycle fatigue life

The LCF lives of the HEA samples with different microstructures are summarized in Fig. 8 and Table 1. As expected, the increased strain amplitude generates the deterioration of fatigue life. Moreover, the fatigue life is significantly influenced by the shell fraction. It is noteworthy that the HS samples exhibit higher fatigue life than CG samples at $\Delta\varepsilon/2 = 0.3$ %. Especially, all samples have a similar fatigue life at $\Delta\varepsilon/2 = 0.4$ % or 0.5 %. However, when the stain amplitude increases to 0.7 %, the HS samples with $S_f = 46.8$ % show much worse fatigue life than the other samples. Overall, the fatigue life is enhanced in the HS samples at low strain amplitude, while fatigue life is deteriorated at high strain amplitude.

3.4. Microstructure evolution during low cycle fatigue process

In order to reveal the difference of cyclic stress response between CG samples and HS samples, the dislocations evolution is illustrated in Figs. 9–11. Fig. 9 shows the representative morphology of dislocations in CG samples during LCF process. There are still a few residual dislocations in the SPS sintered CG samples. By contrast, plenty of dislocations pile up in the first 10 cycles, which induces the rapid initial cyclic hardening. With prolonged cycles, the dislocations rearrange to form the dislocation walls with low energy and stable structure at half-life cycle ($N_f/2$). Thus, the cyclic softening appears. The evolution of dislocations in CG CoCrFeMnNi HEAs during LCF process is similar with that in austenitic stainless steels with FCC structure [57].

Fig. 10 presents the morphology of dislocations in the HS samples with $S_f = 46.8$ % before and after LCF process at $\Delta\varepsilon/2 = 0.3$ %. As illustrated in Fig. 2, the HS CoCrFeMnNi HEAs has the gradient shell region. It is interesting to note that the inhomogeneous dislocations also pile up in the core–shell structure. Fig. 10a shows the evolution of dislocations in the core region (CG structure), which is similar with that in the homogeneous CG samples. Namely, the dislocations develop rapidly in the first stage of cycles, and then rearrangement of dislocations appears by the prolonged cycles. By contrast, the evolution of dislocations in the transition region is illustrated in Fig. 10b. The grain size of transition region approximately ranges from 1 μm to 3 μm. It is seen that the dislocations increase significantly in the first 10 cycles, while the annihilation and rearrangement of dislocations is not significant with the continuously increasing cycles. Unlike the core region, the dislocation wall does not form in the transition region. Fig. 10c presents the morphology of dislocations in the shell region (UFG structure). Compared with core region and transition region, although the HS samples with $S_f = 46.8$ % has a large number of UFG structure, a relatively low density of dislocations still appears in the shell region. Moreover, the grain coarsening is not significant during the whole LCF process, indicating that the shell region is stable.

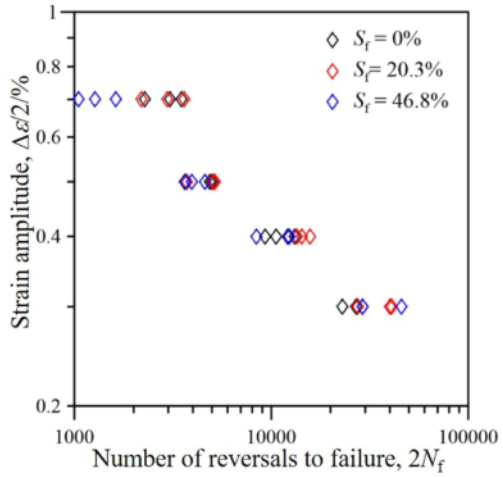

Fig. 8. Plots of strain amplitude ($\Delta\varepsilon/2$) versus the number of cycles to failure (N_f) in the CoCrFeMnNi HEAs with different microstructures.

Table 1
Fatigue lives of the CoCrFeMnNi HEAs with different microstructures.

S_f	N_f			
	$\Delta\varepsilon/2 = 0.3$ %	$\Delta\varepsilon/2 = 0.4$ %	$\Delta\varepsilon/2 = 0.5$ %	$\Delta\varepsilon/2 = 0.7$ %
0 %	13,724	6568	2506	1748
	13,469	5286	2438	1527
	11,474	4661	1822	1141
20.3 %	20,412	7869	2581	1802
	20,033	7126	2536	1480
	13,638	6735	1861	1099
46.8 %	22,944	6153	2300	812
	14,548	6050	1972	635
	14,505	4193	1826	524

Fig. 11 presents the morphology of dislocations in the HS samples with $S_f = 46.8$ % after LCF process at $\Delta\varepsilon/2 = 0.7$ %. As indicated in Fig. 11a, the dislocations pile up significantly and rearrange with increasing cyclic loading in the core region. As shown in Fig. 8, the HS samples with $S_f = 46.8$ % has very short fatigue life. Thus, it is noted that only a few dislocations generate in the transition region (see Fig. 11b). Meanwhile, the cyclic loading seldom promotes the dislocations in the shell region (see Fig. 11c).

In order to reveal the effect of harmonic structure topology on LCF life, fatigue crack initiation in both CG and HS samples after fatigue failure are illustrated in Figs. 12–14. Fig. 12 shows the surface morphologies of CG samples after LCF failure. It is seen from Fig. 12a that a few slip bands form in the interior of several CG grains at $\Delta\varepsilon/2 = 0.3$ %. The extrusions/intrusions along slip bands generate the local stress concentration during LCF process, inducing the fatigue crack initiation. As the strain amplitude increases from 0.3 % to 0.7 %, the increased strain amplitude induces much more slip bands in the interior of CG grains, and multiple cracks initiate along the slip bands (see Fig. 12b).

Fig. 13 shows the surface morphologies of HS samples with $S_f = 20.3$ % after LCF failure. As shown in Fig. 13a and b, it is noted that multiple cracks initiate in the core regions due to the extrusions/intrusions along slip bands at $\Delta\varepsilon/2 = 0.3$ %, which is similar with crack initiation in CG samples. While, no significant slip bands and crack initiation appear in the shell regions. On the contrary, it is interesting to note that the cracks initiate in both core and shell regions at $\Delta\varepsilon/2 = 0.7$ % (see Fig. 13c). As shown in Fig. 13d, the multiple cracks initiate in the shell and at shell/core interface. Therefore, it indicates that the increased strain amplitude promotes incompatible deformation between shell and core regions during LCF process. The local stress concentration increases in the shell and at shell/core interface, generating the crack initiation at multiple sites.

Furthermore, the surface morphologies HS samples with $S_f = 46.8$ % after LCF failure is shown in Fig. 14. Although the fraction of UFG structure increases significantly, it is interesting to note that the fatigue cracks still dominantly initiate along the slip bands in the core region at $\Delta\varepsilon/2 = 0.3$ % (see Fig. 14a and b). Besides core region, it is noted that many cracks also initiate in the shell region and at shell/core interface as the strain amplitude increases from 0.3 % to 0.7 %. The crack initiation in the HS samples with $S_f = 20.3$ % is similar with that in the HS samples with $S_f = 46.8$ % at $\Delta\varepsilon/2 = 0.3$ %. However, due to the large fraction of UFG structure, the HS samples with $S_f = 46.8$ % have more crack initiation sites than the HS samples with $S_f = 20.3$ % at $\Delta\varepsilon/2 = 0.7$ %.

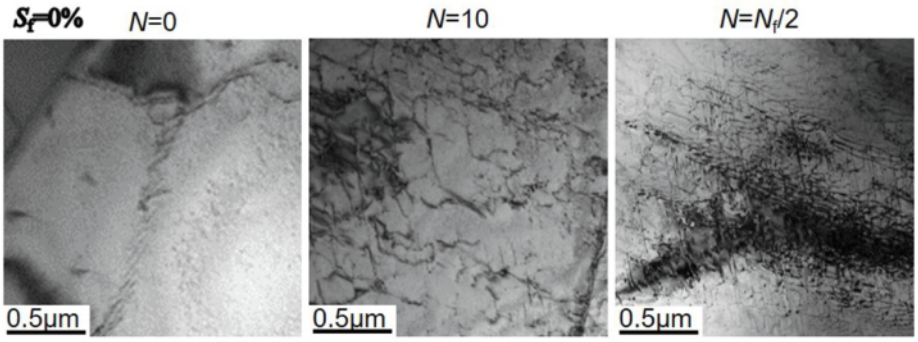

Fig. 9. Representative morphology of dislocations in CG CoCrFeMnNi HEAs ($S_f = 0$ %) at $\Delta\varepsilon/2 = 0.3$ % using TEM.

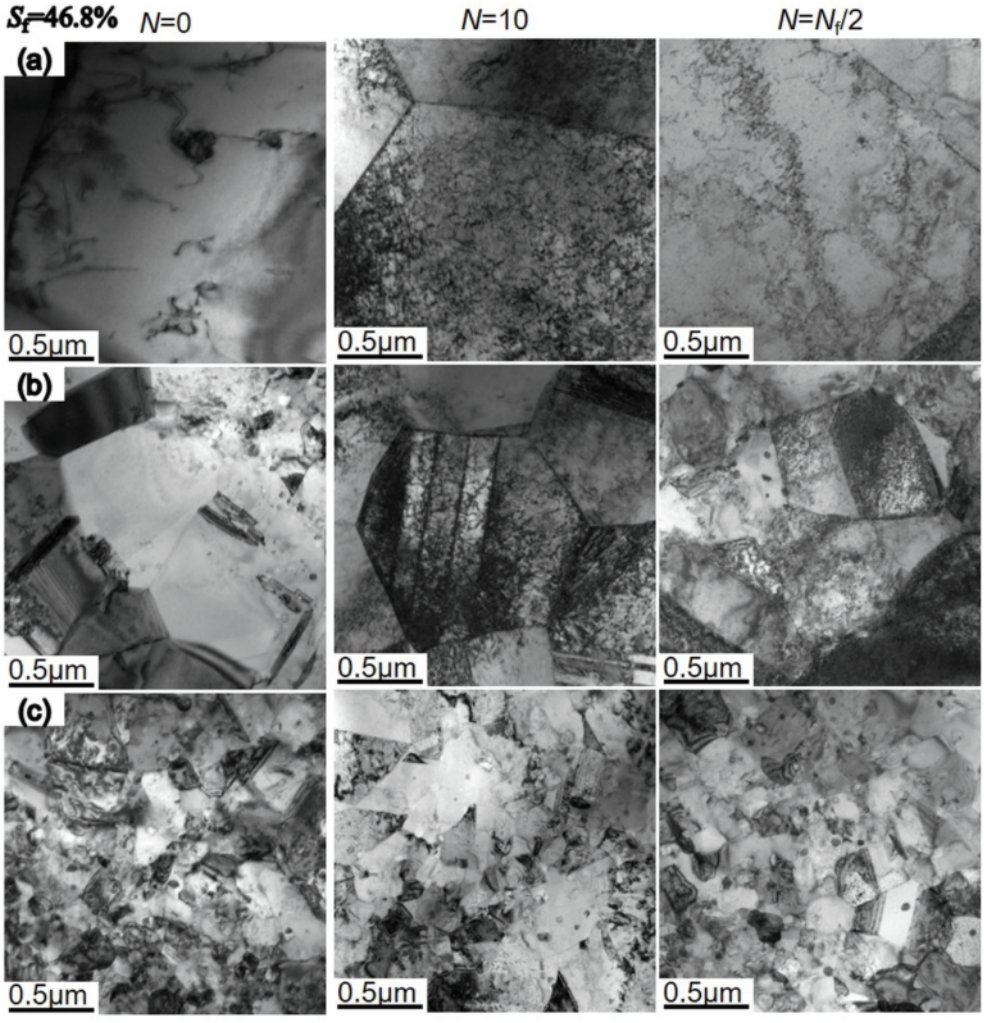

Fig. 10. Representative morphology of dislocations in the HS CoCrFeMnNi HEAs ($S_f = 46.8$ %) at $\Delta\varepsilon/2 = 0.3$ % using TEM: (a) core region; (b) core–shell transition region; (c) shell region.

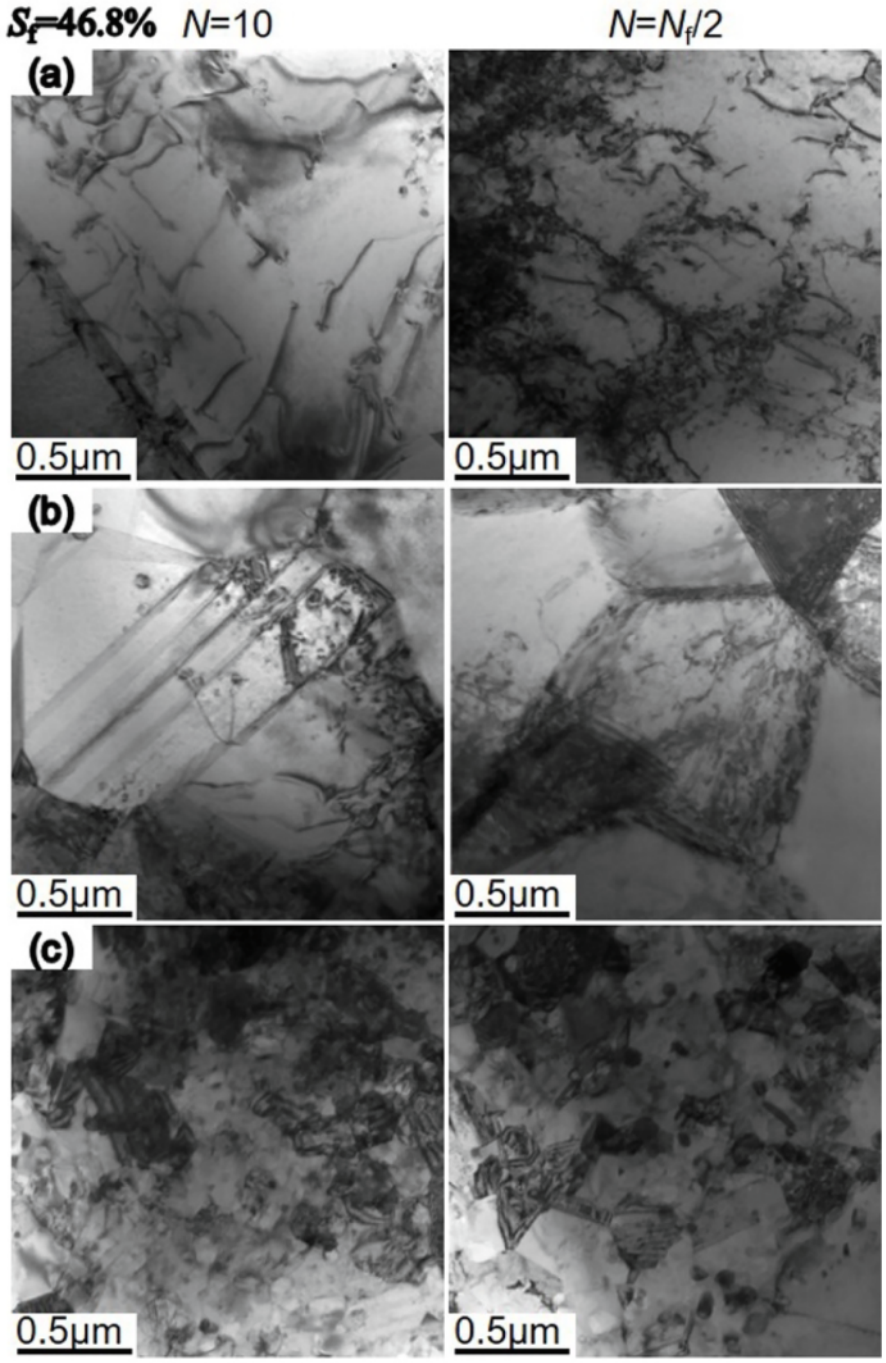

Fig. 11. Representative morphology of dislocations in the HS CoCrFeMnNi HEAs ($S_f = 46.8\,\%$) at $\Delta\varepsilon/2 = 0.7\,\%$ using TEM: (a) core region; (b) core–shell transition region; (c) shell region.

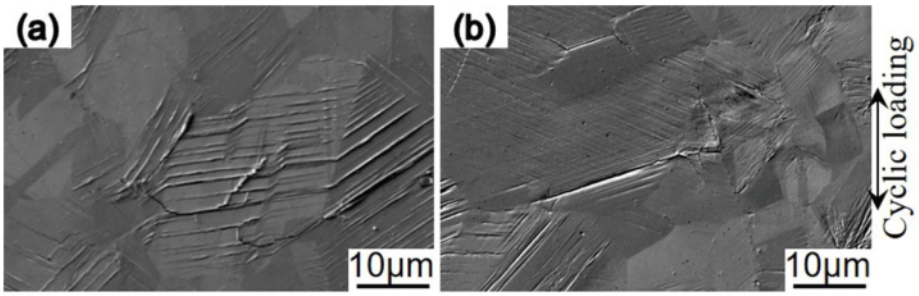

Fig. 12. Surface morphologies of CG CoCrFeMnNi HEAs after LCF failure at different strain amplitudes using SEM: (a) $\Delta\varepsilon/2 = 0.3$ %; (b) $\Delta\varepsilon/2 = 0.7$ %.

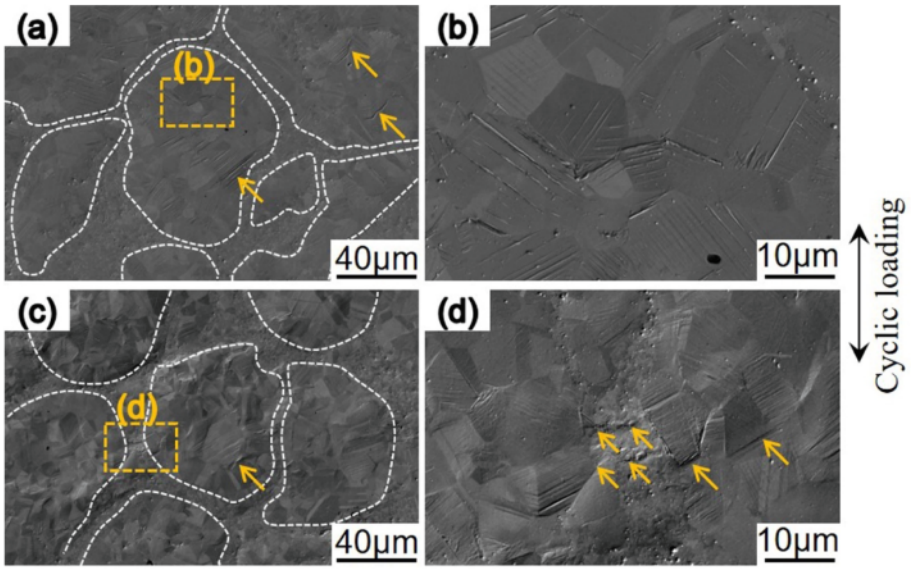

Fig. 13. Surface morphologies of the HS CoCrFeMnNi HEAs with $S_f = 20.3$ % after LCF failure at different strain amplitudes using SEM: (a) $\Delta\varepsilon/2 = 0.3$ % and (b) enlarged region in core; (c) $\Delta\varepsilon/2 = 0.7$ % and (d) enlarged region in shell. The arrows indicate the crack initiation sites.

4. Discussion

4.1. Effect of core–shell grain structure topology on cyclic deformation behavior

The comparison of monotonic and cyclic stress–strain curves between CG and HS samples is illustrated in Fig. 15. Engineering stress and strain values are used for monotonic curves, and cyclic values are obtained from the half-life cycles. It is noted that both CG and HS samples are cyclic softening materials at low strain amplitude ($\Delta\varepsilon/2 = 0.3$ %), while they are cyclic hardening materials at high strain amplitude ($\Delta\varepsilon/2 = 0.7$ %) [58]. Moreover, the cyclic strength coefficient (K') and cyclic strength exponent (n') of CG and HS samples are calculated from the Eq. (3) and summarized in Table 2.

$$\frac{\Delta\sigma}{2} = K'\left(\frac{\Delta\varepsilon_p}{2}\right)^{n'} \tag{3}$$

where $\Delta\sigma/2$ is stress amplitude and $\Delta\varepsilon_p/2$ is plastic strain amplitude at half-life cycle. As shown in Table 2, both K' and n' increase gradually with increasing shell fraction, indicating that the HS samples exhibit much higher cyclic hardening than CG sample. Moreover, the increased shell fraction enhances the cyclic hardening. In general, the UFG materials often shows significant cyclic softening at high strain amplitude [26,33,34]. However, it is noteworthy that although the HS samples have a large number of UFG structure and demonstrate much higher cyclic stress than CG samples, they are still cyclic hardening materials at high strain amplitude ($\Delta\varepsilon/2 = 0.7$ %), indicating that the harmonic structure is stable under cyclic loading.

As illustrated in Fig. 5, it is interesting to note that the shell fraction has significant influence on initial cyclic hardening. With increasing shell fraction, the initial cyclic hardening decreases significantly. It is noted from Figs. 10 and 11 that the dislocation generation and rearrangement dominantly in the core region, which is related to the initial cyclic hardening and cyclic softening. Because the initial cyclic hardening is dependent on the dislocation generation in the CG structure, thus HS samples cannot provide many CG structure for piling up and accumulation of dislocations as the shell fraction increases, restricting the initial cyclic hardening. Subsequently, planar and cross-slip promote the formation of high density dislocation walls and cell-structure, generating the cyclic softening [28,29]. However, it seems that the cyclic softening is independent on the shell fraction, indicating that the following rearrangement of dislocation structure is similar. Moreover, the cyclic induced martensite transformation is not significant in the CG CoCrFeMnNi HEAs during LCF process. Unlike stainless steel, the secondary hardening is not obvious in the CG CoCrFeMnNi HEAs near final

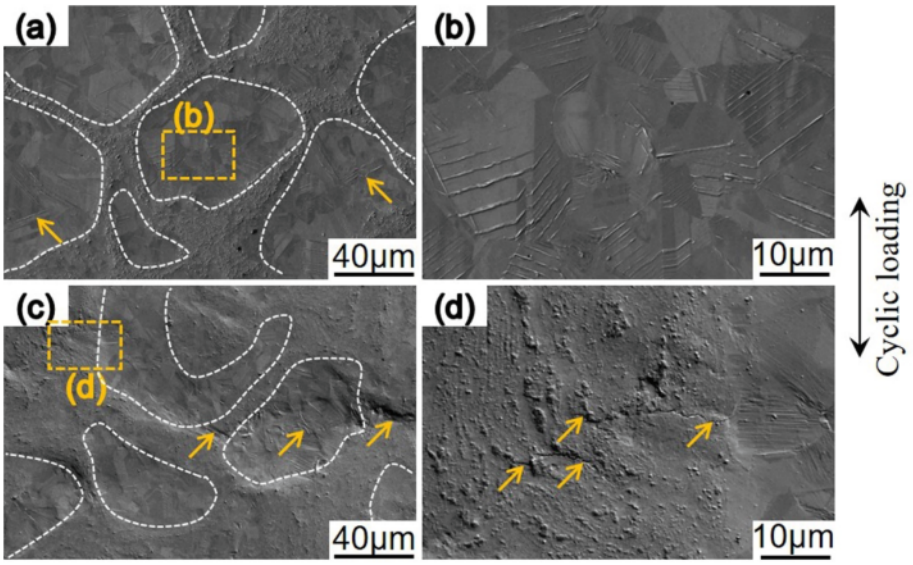

Fig. 14. Surface morphologies of the HS CoCrFeMnNi HEAs with S_f = 46.8 % after LCF failure at different strain amplitudes using SEM: (a) $\Delta\varepsilon/2$ = 0.3 % and (b) enlarged region in core; (c) $\Delta\varepsilon/2$ = 0.7 % and (d) enlarged region in shell. The arrows indicate the crack initiation sites.

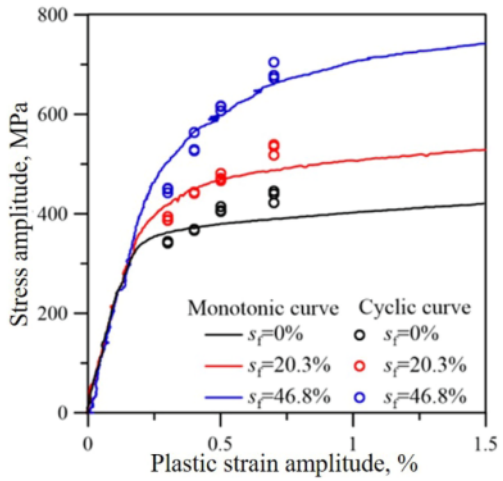

Fig. 15. Comparison of monotonic and cyclic stress–strain curves of CoCrFeMnNi HEAs with different microstructures.

Table 2
Summarized cyclic parameters of CoCrFeMnNi HEAs with different microstructures.

S_f /%	K' /MPa	n'
0	1277	0.2006
20.3	1817	0.2273
46.8	3850	0.3025

fracture [28]. In the present work, there is no significant martensite transformation in the cyclic deformed HS CoCrFeMnNi HEAs. Thus, the HS CoCrFeMnNi HEAs has no significant secondary hardening.

Owing to the different hardness between CG and UFG structure, plastic strain generation is inhomogeneous in the heterogeneous grain structured materials during cyclic loading. It is observed that the cyclic plastic strain dominantly appears in the relatively soft domain prior to the hard domain with smaller grain size and higher cyclic stress. Then, the plastic strain gradually propagates from the soft domain to the hard domain with continuously increasing cyclic loading. Therefore, the fatigue induced strain incompatibility occurs in the NG and UFG layer in gradient structure [33,34]. In the present work, the core region with CG structure is softer than the shell region with UFG structure. According to Figs. 10 and 11, the fatigue generated dislocation activity dominantly occurs in the soft core region in the HS samples. Thus, the slip bands mainly form in the core region, which are not significant in the shell region. Therefore, it is implied that the cyclic plastic strain in the HS samples is inhomogeneous. The gradient transition region shows a few dislocations, which may provide deformation compatibility. However, based on Figs. 13 and 14, it is noteworthy that the cracks tend to form in the shell region at high strain amplitude ($\Delta\varepsilon/2$ = 0.7 %), while the cracks seldom form in the shell region at low strain amplitude ($\Delta\varepsilon/2$ = 0.3 %), which indicates that the high cyclic stress may promote the propagation of cyclic plastic strain from the core region to the shell region.

It has been reported that the CG CoCrFeMnNi HEA shows non-Masing behavior, indicating that the dislocation activity is depends on the stress amplitude [32]. However, as indicated in Fig. 7, the non-Masing behavior eliminates gradually with increasing shell fraction. The HS sample with large shell fraction (S_f = 46.8 %) shows near Masing behavior, indicating that the change of dislocation activity is slow with increasing stress amplitude. Because it doesn't allow dislocation activity to adapt to stress amplitudes in the UFG structure, thus the homogeneous UFG materials often show perfect Masing behavior [59]. As illustrated in Figs. 10 and 11, the dislocation activity in the shell region is not obvious even as the strain amplitude increases from 0.3 % to 0.7 %. Namely, the microstructure in the shell is stable regardless of the strain amplitude, which promotes the possibility of Masing behavior in the HS samples. Consequently, the HS sample with large shell fraction (S_f = 46.8 %) shows the near Masing behavior, which means that the change of dislocation activity is slow with increasing stress amplitude. Furthermore, the shear bands or grain-coarsening tend to occur in the UFG materials during fatigue loading [60,61]. It is noted that both of them does not appear in the HS samples during LCF process. Therefore,

compared with conventional UFG structure, the HS topology shows much stable against fatigue loading.

4.2. Effect of core–shell grain structure topology on LCF resistance

The effect of grain size on LCF life of CoCrFeMnNi HEAs with homogeneous grain structure has been summarized over the past few years [31]. It is noted that the UFG CoCrFeMnNi HEAs show the better fatigue life than CG CoCrFeMnNi HEAs at low strain amplitude (<0.3 %). While, the inferior fatigue life tends to occur as the strain amplitude is over 0.5 %. It is well-known that the resistance to crack initiation can be enhanced by grain refinement, thus the UFG CoCrFeMnNi HEAs exhibits the superior fatigue life at low strain amplitude (<0.3 %). However, the plastic deformation capability deteriorates significantly in the UFG CoCrFeMnNi HEAs. The increased strain amplitude promotes the dynamic grain refinement and cyclic softening effect, which is harmful to fatigue life. Therefore, the deterioration of fatigue life easily appears in UFG CoCrFeMnNi HEAs with increasing strain amplitude [30]. By contrast, it is noticeable that the high strain amplitude also promotes twinning in the FG CoCrFeMnNi HEAs during LCF process, which enhances the plastic deformation capability, generating a positive effect on extending the fatigue life. Therefore, the combined effects of grain refinement and twinning-induced cyclic deformation generate the higher fatigue life in FG CoCrFeMnNi HEAs (18 μm) compared with CG CoCrFeMnNi HEAs (184 μm) [31].

As illustrated in Fig. 8 and Table 1, it is noted that strain amplitude plays an important role on LCF life of HS CoCrFeMnNi HEAs. The fatigue life of HS samples exhibits a slightly higher fatigue life than CG samples at low strain amplitude ($\Delta\varepsilon/2 = 0.3$ %). Owing to UFG structure, the strength of HS samples is increased significantly, which also enhances the resistance to crack initiation, prolonging the fatigue life at low strain amplitude. It is well-known that there is a trade-off between the strength and ductility. The enhanced strength usually induces the deterioration of plastic deformation capability and the enhanced cyclic stress also generates high energy dissipation during LCF process, leading to an inferior fatigue life in the materials with homogeneous grain structure [57]. On the contrary, although the ductility deteriorates gradually with increasing shell fraction in the HS samples, it is noteworthy that both HS samples and CG samples have the similar fatigue life as the strain amplitudes are 0.4 % and 0.5 %. The inferior fatigue life only occurs in the HS samples with $S_f = 46.8$ % at high strain amplitude ($\Delta\varepsilon/2 = 0.7$ %).

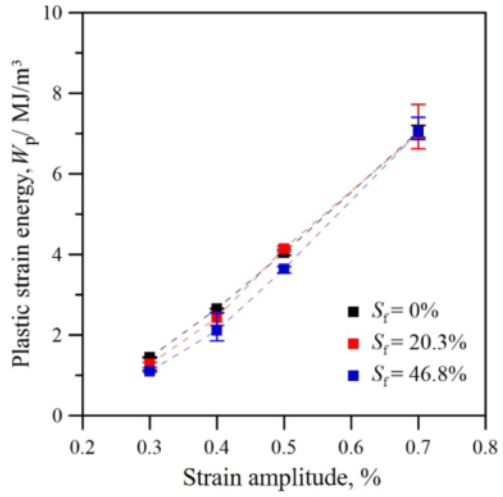

Fig. 16. Energy dissipation of CoCrFeMnNi HEAs with different microstructures obtained from the half-life hysteresis loop.

Fig. 16 shows the effect of strain amplitude on energy dissipation of CoCrFeMnNi HEAs with different shell fractions. It is noted that the shell fraction has insignificant influence on energy dissipation during LCF process. As shown in Fig. 6, although the peak cyclic stress of HS samples increases gradually with increasing shell fraction, the plastic strain amplitude decreases simultaneously. Overall, compared with CG samples, the change of energy dissipation in the HS samples is not significant. Unlike homogeneous UFG materials, it is noted from Fig. 5 that the HS samples does not exhibit rapid cyclic softening at high strain amplitude. The grain coarsening is not significant in the UFG structure. Moreover, the core–shell structure topology provides the HDI hardening and enhances the ductility, which is also beneficial for LCF resistance [50]. Therefore, it is implied that the combined effects of grain refinement and enhanced ductility provide a great LCF resistance in the HS CoCrFeMnNi HEAs.

Compared with shell fraction, the strain amplitude has much more pronounced influence on fatigue crack initiation. Based on the experiment observation, the schematic of LCF induced crack initiation in the HS CoCrFeMnNi HEAs under different strain amplitudes is illustrated in Fig. 17. The plastic deformation dominantly locates in the core regions at low strain amplitude ($\Delta\varepsilon/2 = 0.3$ %), wherein the fatigue cracks initiate due to the extrusions/intrusions along slip bands. Owing to the regular core–shell structure topology, the crack initiation in the multiple core regions can be observed in the gauge area. Moreover, the increased cyclic stress may promote the propagation of plastic strain from core regions to shell regions. Thus, it is remarkable that multiple cracks also initiate in the shell region and at core/shell interface at high strain amplitude ($\Delta\varepsilon/2 = 0.7$ %) besides core regions. The shell region has much poorer resistance to fatigue crack propagation than the core region. Therefore, it is implied that the inferior fatigue life in the HS CoCrFeMnNi HEAs with $S_f = 46.8$ % at high strain amplitude ($\Delta\varepsilon/2 = 0.7$ %) is also attributed to the initiation and propagation of the multiple fatigue cracks in the shell region.

It is noteworthy that although the elongation of HS CoCrFeMnNi HEAs with $S_f = 46.8$ % reduces to approximately one-third of CG samples, the HS samples still demonstrate a similar or higher fatigue life as compared to CG samples when $\Delta\varepsilon/2 < 0.5$ %. According to the literature [34], the fatigue resistance can be enhanced in the heterogeneous structured materials by suppressing the strain localization and damage accumulation. Based on our investigations, the combined effects of grain refinement and stable cyclic deformation behavior are expected to enhance the LCF life in the CoCrFeMnNi HEAs. Therefore, it is implied that optimizing the heterogeneous grain structure topology may be an effective method to enhance the LCF resistance of CoCrFeMnNi HEAs.

5. Conclusions

In the present work, the low cycle fatigue behavior of CoCrFeMnNi HEAs with core–shell heterogeneous grain structure were investigated under different strain amplitudes at room temperature. The effects of core–shell network structure topology on cyclic response, cyclic deformation mechanism and fatigue life were discussed. The main conclusions are summarized as follows:

(1) The shell fraction has significant influence on initial cyclic hardening, while it has insignificant influence on the subsequent cyclic softening. The initial cyclic hardening is restrained by increasing shell fraction. Compared with CG samples, the Masing behavior is also enhanced with increasing shell fraction.

(2) The generation and rearrangement of dislocations dominantly occur in the core region, while the shell region has low density of dislocations during LCF process. The inhomogeneous activity of dislocations implies that the plastic deformation may dominantly appear in the soft core region prior to the hard shell region during LCF process.

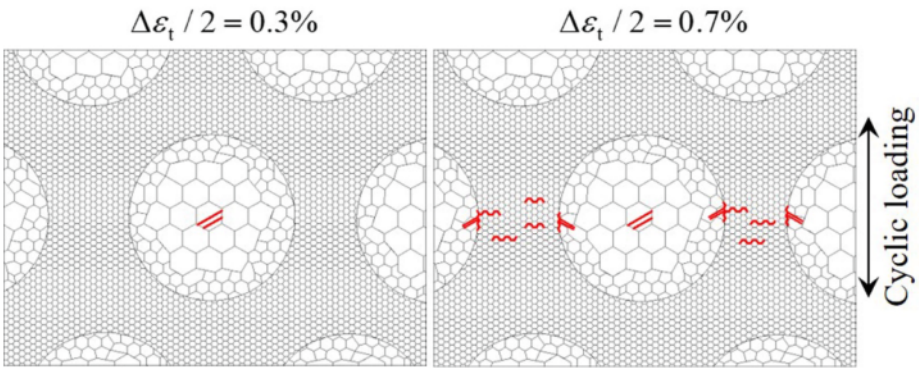

Fig. 17. Schematic of the fatigue crack initiation in HS CoCrFeMnNi HEAs under different strain amplitudes.

(3) The fatigue crack initiation of HS samples is different under different strain amplitudes. The fatigue cracks dominantly initiate in the core region at low strain amplitude ($\Delta\varepsilon/2 = 0.3$ %). While, the multiple cracks initiate in the shell region and at core/shell interfaces at high strain amplitude ($\Delta\varepsilon/2 = 0.7$ %). It implies that the high cyclic stress promotes the propagation of cyclic deformation from the core region to the shell region.

(4) Although the ductility of the HS samples deteriorates significantly with increasing shell fraction, the LCF resistance still remains when the strain amplitude is below 0.5 %. The combined effects of grain refinement and enhanced ductility are expected to enhance the LCF resistance. Our investigations deepen the understanding of LCF behavior of heterogenous structured HEAs and may provide insights on designing fatigue-resistant materials.

CRediT authorship contribution statement

Zhe Zhang: Conceptualization, Data curation, Funding acquisition, Resources, Supervision, Writing – original draft. **Xinyu Zhai:** Investigation, Methodology, Visualization. **Lydia Anggraini:** Funding acquisition, Methodology, Writing – review & editing. **Bo Zhang:** Investigation. **Yushan Ma:** Conceptualization, Project administration. **Kei Ameyama:** Supervision. **Xu Chen:** Project administration, Resources, Supervision.

Declaration of competing interest

The authors declare that they have no known competing financial interests or personal relationships that could have appeared to influence the work reported in this paper.

Data availability

Data will be made available on request.

Acknowledgments

This work was partially supported by the National Natural Science Foundation of China (52075368, 51605325) and the World Class Professor Program from the Directorate General of Higher Education, Research and Technology of the Indonesian Ministry of Education, Culture, Research, and Technology, based on decree No. 2808/E4/DT.04.03/2023 under the budget of Indonesia Endowment Fund for Education.

References

[1] Gludovatz B, Hohenwarter A, Catoor D, Chang EH, George EP, Ritchie RO. A fracture-resistant high-entropy alloy for cryogenic applications. Science 2014;345:1153–8.
[2] Otto F, Dlouhý A, Somsen C, Bei H, Eggeler G, George EP. The influences of temperature and microstructure on the tensile properties of a CoCrFeMnNi high entropy alloy. Acta Mater 2013;61:5743–55.
[3] Wang J, Zhang Z, Dai H, Fujiwara H, Chen X, Ameyama K. Enhanced corrosion resistance of CoCrFeMnNi high entropy alloy using heterogeneous structure design. Corros Sci 2022;209:110761.
[4] Joseph J, Haghdadi N, Annasamy M, Kada S, Hodgson PD, Barnett MR, et al. On the enhanced wear resistance of CoCrFeMnNi high entropy alloy at intermediate temperature. Scr Mater 2020;186:230–5.
[5] Zhu YT, Wu X. Heterostructured materials. Prog Mater Sci 2023;131:101019.
[6] Romero-Resendiz L, El-Tahawy M, Zhang T, Rossi MC, Marulanda-Cardona DM, Yang T, et al. Mater. Sci. Eng. R 2022;150:100691.
[7] Zhu YT, Ameyama K, Anderson PM, Beyerlein IJ, Gao H, Kim HS, et al. Heterostructured materials: superior properties from hetero-zone interaction. Mater. Res. Lett. 2021;9:1–31.
[8] Liu XC, Zhang HW, Lu K. Strain-induced ultrahard and ultrastable nanolaminated structure in nickel. Science 2013;342:337–40.
[9] Lu K. Making strong nanomaterials ductile with gradients. Science 2014;345:1455–6.
[10] Zheng R, Liu M, Zhang Z, Ameyama K, Ma C. Towards strength-ductility synergy through hierarchical microstructure design in an austenitic stainless steel. Scr Mater 2019;169:76–81.
[11] Shi S, Zhang Z, Wang X, Zhou G, Xie G, Wang D, et al. Microstructure evolution and enhanced mechanical properties in SUS316LN steel processed by high pressure torsion at room temperature. Mater Sci Eng A 2018;711:476–83.
[12] Sathiyamoorthi P, Kim HS. High-entropy alloys with heterogeneous microstructure: Processing and mechanical properties. Prog Mater Sci 2022;123:100709.
[13] Pan Q, Zhang L, Feng R, Lu Q, An K, Chuang AC, et al. Gradient cell–structured high-entropy alloy with exceptional strength and ductility. Science 2021;374:984–9.
[14] An Z, Mao S, Liu Y, Zhou H, Zhai Y, Tian Z, et al. Hierarchical grain size and nanotwin gradient microstructure for improved mechanical properties of a non-equiatomic CoCrFeMnNi high-entropy alloy. J Mater Sci Technol 2021;92:195–207.
[15] Chen L, Cao T, Wei R, Tang K, Xin C, Jiang F, et al. Gradient structure design to strengthen carbon interstitial $Fe_{40}Mn_{40}Co_{10}Cr_{10}$ high entropy alloys. Mater Sci Eng A 2020;772:138661.
[16] Ren J, Zhang Y, Zhao D, Chen Y, Guan S, Liu Y, et al. Strong yet ductile nanolamellar high-entropy alloys by additive manufacturing. Nature 2022;608:62–8.
[17] Su J, Raabe D, Li Z. Hierarchical microstructure design to tune the mechanical behavior of an interstitial TRIP-TWIP high-entropy alloy. Acta Mater 2019;163:40–54.
[18] Zhang C, Zhu C, Harrington T, Vecchio K. Design of non-equiatomic high entropy alloys with heterogeneous lamella structure towards strength-ductility synergy. Scr Mater 2018;154:78–82.
[19] Zhang Z, Ma H, Zheng R, Hu Q, Nakatani M, Ota M, et al. Fatigue behavior of a harmonic structure designed austenitic stainless steel under uniaxial stress loading. Mater Sci Eng A 2017;707:287–94.
[20] Zhou G, Ma H, Zhang Z, Sun J, Wang X, Zeng P, et al. Fatigue crack growth behavior in a harmonic structure designed austenitic stainless steel. Mater Sci Eng A 2019;758:121–9.
[21] Zare Ghomsheh M, Khatibi G, Weiss B, Lederer M, Schwarz S, Steiger-Thirsfeld A, et al. High cycle fatigue deformation mechanisms of a single phase CrMnFeCoNi high entropy alloy. Mater Sci Eng A 2020;777:139034.

[22] Kim Y, Ham G, Kim HS, Lee K. High-cycle fatigue and tensile deformation behaviors of coarse-grained equiatomic CoCrFeMnNi high entropy alloy and unexpected hardening behavior during cyclic loading. Intermetallics 2019;111:106486.
[23] Tian YZ, Sun SJ, Lin HR, Zhang ZF. Fatigue behavior of CoCrFeMnNi high-entropy alloy under fully reversed cyclic deformation. J Mater Sci Technol 2019;35:334–40.
[24] Li W, Chen S, Liaw PK. Discovery and design of fatigue-resistant high-entropy alloys. Scr Mater 2020;187:68–75.
[25] Ueno H, Kakihata K, Kaneko Y, Hashimoto S, Vinogradov A. Enhanced fatigue properties of nanostructured austenitic SUS316L stainless steel. Acta Mater 2011;59:7060–9.
[26] Mughrabi H, Höppel HW. Cyclic deformation and fatigue properties of very fine-grained metals and alloys. Int J Fatigue 2010;32:1413–27.
[27] Vinogradov A, Yasnikov LS, Matsuyama H, Uchida M, Kaneko Y, Estrin Y. Controlling strength and ductility: dislocation-based model of necking instability and its verification for ultrafine grain 316L steel. Acta Mater 2016;57(106):295–303.
[28] Shams SAA, Jang G, Won JW, Bae JW, Jin H, Kim HS, et al. Low-cycle fatigue properties of CoCrFeMnNi high-entropy alloy compared with its conventional counterparts. Mater Sci Eng A 2020;792:139661.
[29] Lu K, Chauhan A, Tirunilai AS, Freudenberger J, Kauffmann A, Heilmaier M, et al. Deformation mechanisms of CoCrFeMnNi high-entropy alloy under low-cycle-fatigue loading. Acta Mater 2021;215:117089.
[30] Picak S, Wegener T, Sajadifar SV, Sobrero C, Richter J, Kim H, et al. On the low-cycle fatigue response of CoCrNiFeMn high entropy alloy with ultra-fine grain structure. Acta Mater 2021;205:116540.
[31] Luo M, Lam T, Wang P, Tsou N, Chang Y, Feng R, et al. Grain-size-dependent microstructure effects on cyclic deformation mechanisms in CoCrFeMnNi high-entropy-alloys. Scr Mater 2022;210:114459.
[32] Shams SAA, Kim G, Won JW, Kim JN, Kim HS, Lee CS. Effect of grain size on the low-cycle fatigue behavior of carbon-containing high-entropy alloys. Mater Sci Eng A 2021;810:140985.
[33] Pan Q, Long JZ, Jing LJ, Tao NR, Lu L. Cyclic strain amplitude-dependent fatigue mechanism of gradient nanograined Cu. Acta Mater 2020;196:252–60.
[34] Pan Q, Lu L. Improved fatigue resistance of gradient nanograined metallic materials: Suppress strain localization and damage accumulation. Scr Mater 2020;187:301–6.
[35] Ho HS, Zhou WL, Li Y, Liu KK, Zhang E. Low-cycle fatigue behavior of austenitic stainless steels with gradient structured surface layer. Int J Fatigue 2020;134:105481.
[36] Liu Y, Chen H, Wang R, Jia Y, Zhang X, Cui Y, et al. Fatigue behaviors of 2205 duplex stainless steel with gradient nanostructured surface layer. Int J Fatigue 2021;147:106170.
[37] Lu K, Knöpfle F, Chauhan A, Jeong HT, Litvinov D, Walter M, et al. Low-cycle fatigue behavior and deformation mechanisms of a dual-phase $Al_{0.5}$CoCrFeMnNi high-entropy alloy. Int J Fatigue 2022;163:107075.
[38] Bahadur F, Jain R, Biswas K, Gurao NP. Low cycle fatigue behaviour of non-equiatomic TRIP dual-phase $Fe_{50}Mn_{30}Co_{10}Cr_{10}$ high entropy alloy. Int J Fatigue 2022;155:106545.
[39] Ameyama K, Cazes F, Couque H, Dirras G, Kikuchi S, Li J, et al. Harmonic structure, a promising microstructure design. Mater Res Lett 2022;10:440–71.
[40] Ovid'ko IA, Valiev RZ, Zhu TY. Review on superior strength and enhanced ductility of metallic nanomaterials. Prog Mater Sci 2018;94:462–540.
[41] Estrin Y, Beygelzimer Y, Kulagin R, Gumbsch P, Fratzl P, Zhu YT, et al. Architecturing materials at mesoscale: some current trends. Mater Res Lett 2021;9:399–421.
[42] Zhang Z, Vajpai SK, Orlov D, Ameyama K. Improvement of mechanical properties in SUS304L steel through the control of bimodal microstructure characteristics. Mater Sci Eng A 2014;598:106–13.
[43] Zhang Z, Orlov D, Vajpai SK, Tong B, Ameyama K. Importance of bimodal structure topology in the control of mechanical properties of a stainless steel. Adv Eng Mater 2015;17:791–5.
[44] Zheng R, Zhang Z, Nakatani M, Ota M, Chen X, Ma C, et al. Enhanced ductility in harmonic structure designed SUS316L produced by high energy ball milling and hot isostatic sintering. Mater Sci Eng A 2016;674:212–20.
[45] Park HK, Kim Y, Park JM, Ameyama K, Kim HS. Efficient design of harmonic structure using an integrated hetero-deformation induced hardening model and machine learning algorithm. Acta Mater 2023;244:118583.
[46] Li G, Jiang J, Ma H, Zheng R, Gao S, Zhao S, et al. Superior strength–ductility synergy in three-dimensional heterogeneous-nanostructured metals. Acta Mater 2023;256:119143.
[47] Nakai Y, Kikuchi S, Osaki K, Kawabata MO, Ameyama K. Effects of rolling reduction and direction on fatigue crack propagation in commercially pure titanium with harmonic structure. Int J Fatigue 2021;143:106018.
[48] Kikuchi S, Nukui Y, Nakatsuka Y, Nakai Y, Nakatani M, Kawabata MO, et al. Effect of bimodal harmonic structure on fatigue properties of austenitic stainless steel under axial loading. Int J Fatigue 2019;127:222–8.
[49] Li G, Liu M, Lyu S, Nakatani M, Zheng R, Ma C, et al. Simultaneously enhanced strength and strain hardening capacity in FeMnCoCr high-entropy alloy via harmonic structure design. Scr Mater 2021;191:196–201.
[50] Zhang Z, Zhai X, Chen G, Chen X, Ameyama K. Enhanced synergy of strength-ductility and low-cycle fatigue resistance of high-entropy alloy through harmonic structure design. Scr Mater 2022;213:114591.
[51] Shi L, Zhang Z, Chen X. Fatigue crack growth behavior in CoCrFeMnNi high entropy alloy with harmonic structure topology. Int J Fatigue 2023;172:107656.
[52] Nagata M, Horikawa N, Kawabata M, Ameyama K. Effects of microstructure on mechanical properties of harmonic structure designed pure Ni. Mater Trans 2019;60:1914–20.
[53] Xu L, Luo X, Zhao L, Han Y, Hao K, Qi X. Study on creep-fatigue response, failure mode and deformation mechanism of 316H steel welded joint. J Mater Sci 2022;57:22099–118.
[54] Li Y, Laird C. Masing behavior observed in monocrystalline copper during cyclic deformation. Mater Sci Eng A 1993;161:23–9.
[55] Wang Z, Laird C. Relationship between loading process and Masing behavior in cyclic deformation. Mater. Sci. Eng. A 101 (1988) LI -L5.
[56] Niendorf T, Wegener T, Li Z, Raabe D. Unexpected cyclic stress-strain response of dual-phase high-entropy alloys induced by partial reversibility of deformation. Scr Mater 2018;143:63–7.
[57] Zhang Z, Li A, Wang YP, Lin Q, Chen X. Low-cycle fatigue behavior and life prediction of fine-grained 316LN austenitic stainless steel. J Mater Res 2020;35:3180–91.
[58] Shamsaei N, Fatemi A, Socie DF. Multiaxial cyclic deformation and non-proportional hardening employing discriminating load paths. Int J Plasticity 2010;26:1680–701.
[59] Niendorf T, Canadinc D, Maier HJ, Karaman I, Sutter SG. On the fatigue behavior of ultrafine-grained interstitial-free steel. Int J Mater Res 2006;97:1328–36.
[60] An XH, Wu SD, Wang ZG, Zhang ZF. Enhanced cyclic deformation responses of ultrafine-grained Cu and nanocrystalline Cu–Al alloys. Acta Mater 2014;74:200–14.
[61] Malekjani S, Hodgson PD, Stanford NE, Hilditch TB. Shear bands evolution in ultrafine-grained aluminium under cyclic loading. Scr Mater 2013;68:821–4.

Turnitin Low cycle fatigue behavior

ORIGINALITY REPORT

10%	7%	11%	2%
SIMILARITY INDEX	INTERNET SOURCES	PUBLICATIONS	STUDENT PAPERS

MATCH ALL SOURCES (ONLY SELECTED SOURCE PRINTED)

3%

★ Tomotsugu Shimokawa, Tatsuya Hasegawa, Keito Kiyota, Tomoaki Niiyama, Kei Ameyama. "Heterogeneous evolution of lattice defects leading to high strength and high ductility in harmonic structure materials through atomic and dislocation simulations", Acta Materialia, 2022

Publication

Exclude quotes	On	Exclude matches	< 1%
Exclude bibliography	On		